Mechanical Systems and Signal Processing 188 (2023) 109951

Contents lists available at ScienceDirect

Mechanical Systems and Signal Processing

journal homepage: www.elsevier.com/locate/ymssp

A multi-degree-of-freedom triboelectric energy harvester for dual-frequency vibration energy harvesting

Zicheng Liu, Chaoyang Zhao, Guobiao Hu, Yaowen Yang [*]

School of Civil and Environmental Engineering, Nanyang Technological University, 50 Nanyang Avenue, 639798, Singapore

ARTICLE INFO

Communicated by: Xingjian Jing

ABSTRACT

Vibrational energy harvesting based on triboelectric transduction has been proven to be a cost-effective solution for powering small electronic sensors. Triboelectric energy harvesters (TEHs) that work in the contact-separation mode have been widely investigated with beam-mass structures. However, most beam-based TEHs utilize cantilever beams as their driving component, which is applicable only when its first mode is excited because higher modal frequencies are usually beyond the range of ambient vibrations. This study presents a novel contact-separation-mode energy harvester that, for the first time, combines triboelectric transduction with a multi-degree-of-freedom (MDOF) L-shaped beam-mass structure to harvest vibration energy at two operating frequencies. The TEH proposed in this study has two operating frequencies under 20 Hz and thus possesses an increased operating frequency range. A fully coupled electromechanical model that combines an MDOF distributed-parameter mechanical model with an electrical model for the TEH is derived. Experiments are then carried out to validate the model, characterize the performance of the TEH, and investigate the effect of the MDOF beam-mass structure on the contact-separation-mode TEH. It is shown that the predictions of the electromechanical model have an overall good agreement with the experimental results. Besides, the TEH can achieve a maximum root-mean-square voltage of 9.45 V when the first mode is excited and 11.56 V when the second mode is excited, given a base excitation acceleration of 0.6 g and the external load resistance of 1 MΩ. An optimal power of 300 μW is realized when the external load is 85 MΩ.

1. Introduction

The development of the Internet of Things (IoT) has led to the mass deployment of small wireless electronic sensors that operate on the micro- to milli-watt scale and require reliable energy sources. Currently, chemical batteries constitute the primary energy source for such sensors, but they need regular replacements, leading to intermittent operation halts. In contrast, continuous and renewable energy sources better ensure their perpetual operations. One such energy source is ambient vibration, which is ubiquitous but often inefficiently utilized. Therefore, much research has been invested into effectively harnessing energy from ambient vibration to power IoT sensors. Mechanisms based on electromagnetic, [1], electrostatic [2], piezoelectric [3,4], and triboelectric [5,6] transductions are the primary foci of research. Among them, harvesters based on triboelectric transduction, or triboelectric energy harvesters (TEH), have received increasing attention since the concept of triboelectric energy harvester was initiated by Wang et al. [7]. Their broad

---

* Corresponding author.
E-mail address: cywyang@ntu.edu.sg (Y. Yang).

https://doi.org/10.1016/j.ymssp.2022.109951
Received 19 September 2022; Received in revised form 30 October 2022; Accepted 11 November 2022

material accessibility, cheap cost, high design flexibility [8], easy fabrication, and high energy-conversion efficiency [9,10] are the primary advantages that draw research attention.

The energy harvesting materials for a TEH are chosen in a pair such that the process of triboelectrification occurs when the two materials are in contact. In this process, one material gains electrons when in contact with the other forming polarized charges in the interface. The pair of materials (triboelectric pair) can be either polymer–polymer or polymer-metal as long as the two materials are of opposite tribo-polarities [11]. Relative motions, either perpendicular or in-plane, between the two materials then induce the charges to flow between the electrodes bonded to the materials due to electrostatic induction [12]. Alternating currents are generated when the motions are cyclic [13]. Four operating modes of TEHs, namely, contact-separation mode, sliding mode, freestanding mode, and single-electrode mode, are recognized [12]. The contact-separation mode (CS-mode) among them is highly flexible as contact-separation cycles between a triboelectric pair can be easily driven by ambient and base vibrations [14–18], whose displacements have components perpendicular to the triboelectric pair's planes. The vibrations in TEHs can also be induced by the wind [19], water waves [20], acoustic-borne vibration [21], etc.

A CS-mode TEHs (CS-TEH) requires a supporting structure that drives the contact-separation cycles between the triboelectric pair when subject to external vibrations. Structures based on elastic components such as springs and beams are commonly used to design TEHs in the literature. Springs have gained much attention in the design of TEHs [16,17,20,22] as they are the intuitive component for providing cyclic motions. However, tuning the mechanical properties of spring-mass structures is challenging as the springs need to be replaced whenever adjustments to their mechanical properties are made. In contrast, the mechanical properties of beam structures are much more easily-tunable as beams are more machinable and flexible. They have gained popularity in piezoelectric energy harvesting in the past decades [23–25] but are given limited attention in designing TEHs. Dhakar et al. investigated using a cantilever beam in the design of a TEH [14] by attaching the polymer-electrode film at the free end of the beam with a metal-film-coated substrate as a mechanical stopper. A similar TEH is reported by Fu et al. [18] with the main beam being placed between two other cantilever beams instead of above a mechanical stopper. For better contact between the triboelectric pair, Zhao et al. proposed a design that utilizes an electrode plate with a rotational degree of freedom that is separated from but driven by the beam [15].

Because ambient vibration spans across a wide range of frequencies, vibration energy harvesters should be able to operate when subject to a wide range of excitation frequencies. The above designs possess impact-induced nonlinearity [14,15,26,27] during operations, leading to the bandwidth-broadening effect. However, this bandwidth-broadening effect is limited and incidental as an inevitable consequence of impact, and these designs are essentially only functional when the first mode of vibration is excited. Thus, more efforts are needed to further expand the operating frequency range of CS-TEHs. Nonetheless, a literature survey can find that such studies are rare. Looking beyond the scope of the CS-mode, Fu et al. proposed a sliding-mode TEH based on a cantilever beam with magnet-induced multistability. Theoretically, they studied the bandwidth-broadening effect due to magnet-induced multistability. However, this design is not validated experimentally, so its performance, in reality, remains to be investigated. In contrast, Gupta et al. designed a spring-based hybrid triboelectric-electromagnetic energy harvester [28] that operates in the CS-mode through four nonlinear polymer springs whose first two natural frequencies are closely located. This prototype has a considerably wider operating bandwidth, but its peak output power generated is relatively small (0.166 μW). Besides, no current published study probes the feasibility of expanding the operating frequencies of TEHs using multimodal structures.

To resolve the lack of investigation in multimodal TEHs with larger operating-frequency range, this paper proposes a novel MDOF TEH that combines an MDOF L-shaped beam-mass structure (LBMS) with a triboelectric energy harvesting unit that operates in the CS-mode for the first time. Although many authors have investigated the L-shaped beam-mass structure in the field of nonlinear dynamics [29,30], and it has been used for piezoelectric harvesters, it has never been used as a driving component for TEHs. Besides, triboelectric and piezoelectric energy harvesters have utterly different operating principles, while the triboelectric ones lead to more complex electromechanical models. The advantage of such an MDOF structure is that, due to its MDOF nature, it can be tuned to have closely located first two natural frequencies [29,31], both of which are within the frequency range of ambient vibrations that are usually less than 50 Hz [32]. Thus, it allows a CS-mode TEH to scavenge vibration energy from a broader frequency spectrum, increasing total operating bandwidth. In the literature, the LBMS is usually tuned to have the second natural frequency being about twice the first ($f_2 \cong 2f_1$) to study or utilize the characteristic of internal resonance [29–31,33]. When $f_2 \cong 2f_1$, f_1 and f_2 can both be within the typical range of ambient vibrations while being relatively close. In contrast, a single cantilever beam without a tip mass already has $f_2 \cong 6.27f_1$ [4]. Adding a tip mass for resonance-frequency tuning will even further increase the gap between f_1 and f_2.

An electromechanical model that fully couples the multi-degree-of-freedom distributed-parameter mechanical model for the LBMS with the electrical model for the non-parallel CS-mode TEH is formulated for the first time. Such a model is needed to determine the design parameters and predict the performance of the L-shaped triboelectric energy harvester (LTEH) so that it can be designed to fit the expected working environments. The model is also validated through experiments, which also investigate the effects of an MDOF structure on a CS-mode triboelectric energy harvesting unit and the effects that certain design parameters have on the energy harvesting performance. The main theoretical development for the electrical model for the CS-mode has been investigated and verified in many studies [11,13,15,18,26]. For the simple case of parallel contact surfaces, the electrical model relates the separation distance (x) with the transferred charge (Q) between the electrodes and the output voltage (V) using Gauss's Law [11]. This relationship is called the V-Q-x relationship. In this study, however, the contact-separation cycles are driven by beams and are non-parallel. Thus, the V-Q-x relationship here is calculated from the total electric-field energy in the gap between the surfaces [15] to account for the non-parallel contact surfaces. Furthermore, a linear distributed parameter mechanical model for the MDOF L-shaped beam is introduced in this study, which initiates the employment of MDOF structures in the theoretical models of TEHs. Many studies in triboelectric energy harvesting neglect the effect of the electrostatic force on the mechanical model induced by the accumulated charge on the contact surfaces [15,18]. However, such a practice leads to a loss in the modeling accuracy, so this study includes the electrostatic force for a completely coupled electromechanical model.

The LBMS has been studied extensively in nonlinear dynamics and exhibits internal resonance when $f_2 \cong 2f_1$ [29–31]. Thus, energy exchange could exist between the first two modes at certain base excitation accelerations when the excitation frequency is near f_1 or f_2 [34]. Nayfeh and Balachandran found that the energy exchange leads to periodic, quasi-periodic, and chaotic responses from the LBMS [29,30]. The effects of internal resonance can potentially influence the performance of a TEH. However, the scope of the theoretical work in this study does not include such a nonlinear phenomenon because the major goal is to utilize more than one vibration mode for energy harvesting. Whether such a phenomenon is present for the LTEH in this study will be discussed in the experimental results.

In summary, the novelty of this study includes pioneering the use of an MDOF dynamical structure in designing a triboelectric energy harvester for dual-frequency vibration-energy harvesting. A coupled electromechanical model incorporating MDOF dynamics is also formulated for the first time to predict the harvester's performance. The rest of this paper is outlined below. The structural design, geometric parameters, and material selection for the LTEH in this study are presented in Section 2. Three main components, the L-shaped beam-mass supporting structure, the triboelectric-pair harvesting unit, and the mechanical stopper, constitute the LTEH. Section 3 then presents the modeling of the electromechanically coupled system. Firstly, the electrical model for the non-parallel triboelectric pair is derived and coupled with the mechanical model for the LBMS. Section 4 then presents the setup for the experiment conducted to validate the model. The parametric study's results are then discussed and compared with the simulated results from the theoretical model. The performance of the LTEH is then demonstrated in a series of characterization experiments. Finally, section 5 finalizes this paper with conclusions.

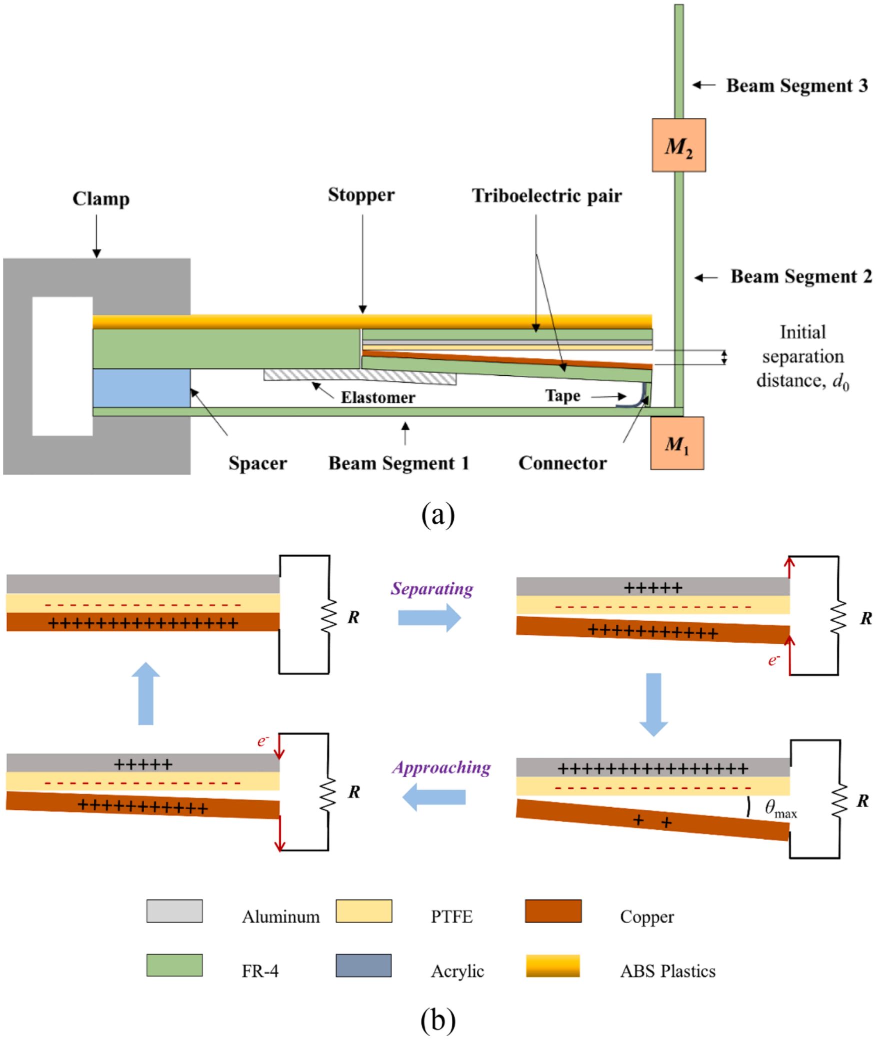

Fig. 1. The configuration of the LTEH: (a) side view of the design scheme, (b) operating mechanism of the harvesting unit.

2. Structural design and operating mechanism

Fig. 1 (a) shows the side view of the designed configuration (not to scale) of the LTEH proposed in this study. One end of the L-shaped beam's horizontal segment (Segment 1) is clamped, while the free end has a tip mass (M_1) attached below. The vertical segment has one end fixed on the free end of beam 1 and has a proof mass (M_2) positioned between the two ends. On the vertical segment, the part between the free end of Segment 1 and M_2 is denoted as Segment 2, while the rest is Segment 3. The L-shaped beam structure is manufactured using the FR-4 glass-reinforced epoxy laminate material because of its high elasticity and electrical insulation. The dimensions of Segments 1, 2, and 3 are 140 mm × 30 mm × 1 mm ($L_1 \times b_1 \times h_1$), 95 mm × 20 mm × 0.6 mm ($L_2 \times b_2 \times h_2$), and 39 mm × 20 mm × 0.6 mm ($L_3 \times b_3 \times h_3$), respectively. A mechanical stopper, which is 3D-printed using ABS plastics, is clamped in parallel with beam 1 and separated by an acrylic block. The stopper is 136 mm × 40 mm × 3 mm in dimension.

An FR-4 glass-reinforced epoxy substrate pasted with an aluminum film and a PTFE layer (Al electrode substrate) is fixed on the unclamped side of the stopper. Another FR-4 substrate pasted with a copper film (Cu electrode substrate) has one end connected to a spacer with a thickness equal to the two substrates' total thickness via an elastomer tape. The elastomer allows the Cu electrode to rotate freely about its left end due to its high flexibility. The free outer (right) end of the Cu electrode has a connector below that is taped near the free end of beam 1 with pliable tape. This way, the PTFE-aluminum film and the copper film comprise a polymer-metal triboelectric pair. The aluminum is the electrode covered by the PTFE layer. The PTFE layer, which is 0.1 mm thick, is used because it displays strong negative tribo-polarity and easily attracts negative charges from materials with positive tribo-polarity or weaker negative tribo-polarity. The copper film serves as both an opposite-tribo-polarity material and an electrode. Both the electrode substrates have a dimension of 105 mm × 40 mm × 1 mm. When the whole beam-mass structure vibrates, the free (right) end tip of Segment 1 drives the Cu electrode to rotate through the connector. When the beam's tip moves up, the outer end of the Cu electrode is pushed up and touches the PTFE layer. The impact with the PTFE layer, which is fixed to the stopper, causes the Cu-electrode to separate from the Al-substrate. Fig. 1 (b) shows the operating mechanism of the triboelectric pair in the energy harvesting unit in which the two electrodes are connected to an external load (R). Initially, starting from the top left, the surface of the PTFE film is negatively charged and in contact with the copper electrode due to the triboelectric effect [35,36]. Due to the insulating properties of the PTFE polymer, the charges acquired on its surface will be retained [36]. The copper electrode then acquires positive charges. As the two surfaces separate, an electric potential builds up in the air gap. This potential causes the electrons to flow from the Al electrode to the Cu electrode until the Al electrode obtains almost all the positive charges from the Cu electrode. At the same time, the separation angle between the triboelectric pair, θ, reaches the maximum. The separation gap then starts closing, and electrons flow from the Cu electrode to the Al electrode since the potential inside the PTFE layer is higher than in the air gap. An alternating current is generated when the beam's vibration drives the rotation cycles on the rotatable Cu electrode.

3. Electromechanical modeling of the LTEH

3.1. The electrical model of the energy harvesting unit

The electrical model presented in this section is established to simulate the voltage output V across the external load R between the two electrodes, as shown in Fig. 2. When the Cu electrode and the PTFE dielectric layer are in contact, the lower surface of the PTFE layer acquires an areal charge density $-\sigma$ through the triboelectric effect. When the two surfaces separate, as shown in Fig. 2, negative charges $-Q$ are transferred from the Al electrode to the Cu electrode due to electrostatic induction caused by the voltage V_a in the air gap. Inside the dielectric layer, a voltage V_d appears due to the positive charges accumulated on the Al electrode. From Gauss's Law, V_d can be expressed as

$$V_d = \frac{-Qh}{A_c \varepsilon_r \varepsilon_0} \tag{1}$$

where Q is the amount of the charges transferred through the external load, h is the thickness of the dielectric layer, A_c is the contact area between the triboelectric pair, is the permittivity of free space, and ε_r is the relative permittivity characteristic of the dielectric

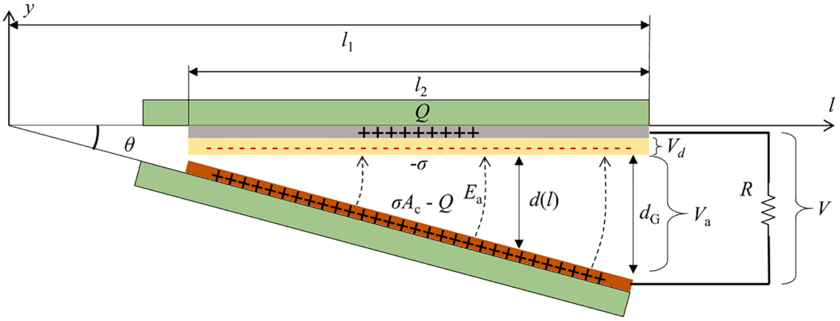

Fig. 2. The detailed schematic electrical model.

material. Gauss's Law cannot be applied here for V_a the same way as that for V_d since the two contact surfaces here are not in parallel. Instead, the method that calculates the air–gap voltage potential from the total electric field energy proposed by Zhao et al. [15] is adopted. The two planes here are assumed to be equipotential, which means the voltage in the air gap at any point along the l-direction is equal. The electric field lines in the air gap along the l-direction are perpendicular to the contact surfaces, so one can integrate along the l-direction to find the total electric field energy as

$$W_e = \int_{l_1-l_2}^{l_1} \frac{\varepsilon_0 E_a}{2} w dl = \int_{l_1-l_2}^{l_1} \frac{\varepsilon_0 V_a^2 w}{2l\theta} dl = \frac{\varepsilon_0 V_a^2 w}{2\theta} \ln\left(\frac{l_1}{l_1-l_2}\right) \tag{2}$$

where w is the width of the contact surfaces, θ is the separation angle between the contact surfaces, l_1 is the distance from the rotation end of the Cu electrode substrate to its outer end, and l_2 is the length of the contact surface between the triboelectric pair. W_e is also related to the total capacitance in the air gap C by

$$W_e = \frac{CV_a^2}{2} = \frac{(\sigma A_c - Q)V_a}{2} \tag{3}$$

Equating the right-hand sides of both Eq (2). and Eq.(3) yields

$$V_a = \frac{\mu(\sigma A_c - Q)\theta}{w\varepsilon_0} = \frac{\mu(\sigma A_c - Q)d_G}{wl_1\varepsilon_0} \tag{4}$$

where μ is the constant coefficient that equals $\left[\ln\left(\frac{l_1}{l_1-l_2}\right)\right]^{-1}$, and d_G is the separation distance between the outer ends of the electrode substrates. The small-angle approximation is used here because $d_G \ll l_1$. From Kirchhoff's voltage law, the governing differential equation for the voltage output on the external load is

$$V = RI(t) = R\frac{dQ(t)}{dt} = V_d + V_a = \frac{\mu[\sigma A_c - Q(t)]d_G(t)}{wl_1\varepsilon_0} - \frac{Q(t)h}{A_c\varepsilon_r\varepsilon_0} \tag{5}$$

It is evident that, in Eq. (5), $d_G(t)$ is the coupling term that relates the motion at the free-end tip of beam Segment 1 in Fig. 1 (a) to the voltage output across R in Fig. 2. The electric field in the air gap E_a leads to the existence of an electrostatic attraction force, F_e, between the two contact surfaces. This force can be found from the infinitesimal voltage in the air gap, dV_a, along the l-direction. This way, the Cu electrode is divided into infinitesimal capacitive plates parallel to the Al electrode. The expression for dV_a is then

$$dV_a = \frac{\mu[\sigma A_c - Q(t)]d_G(t)}{A_c l_1 \varepsilon_0} dl \tag{6}$$

Then the infinitesimal electrostatic force along the l-direction is, from the expression for the electrostatic force between two parallel capacitor plates,

$$dF_e = \frac{[\sigma A_c - Q(t)]}{2d(l)} dV_a = \frac{\mu[\sigma A_c - Q(t)]^2 d_G(t)}{2A_c l_1 l \tan[\theta(t)]\varepsilon_0} dl = \frac{\mu[\sigma A_c - Q(t)]^2}{2A_c l \varepsilon_0} dl \tag{7}$$

where $d(l)$ is the separation distance between the two infinitesimal capacitor plates. Integrating Eq. (7) from $l = l_1 - l_2$ to $l = l_1$ results in the electrostatic force acting perpendicular to the contact surfaces as

$$F_e = \frac{[\sigma A_c - Q(t)]^2}{2A_c\varepsilon_0} \tag{8}$$

$Q(t)$ in the expression for the electrostatic force in Eq. (8) will be used to couple the electrical response to the mechanical model because the electrostatic force will affect the motion near Segment 1′s free-end tip. The parameters used in the electrical model are listed in Table 1.

Table 1
Parameters for the electrical model used in the simulation and experiment.

Parameters	Numerical Values
The permittivity of free space, ε_0	8.85×10^{-12} F · m^{-1}
PTFE layer's relative permittivity, ε_r	2.1
The thickness of the PTFE layer, h	0.1 mm
Length of the contact surface, l_2	105 mm
Width of the contact surface, w	40 mm
Area of the contact surface, A_c	4200 mm^2
Constant coefficient, μ	0.022

3.2. The mechanical model of the L-shaped beam structure

The mechanical model of the LBMS in this study uses a distributed-parameter model. Fig. 1 (a) shows that the Cu-electrode substrate's outer end is taped near the free end of beam Segment 1 through a connector. If the beam displacement at the connection point is large enough such that contact occurs between the triboelectric pair, the connection point of the beam will experience a downward impact force. This study models the impact by treating the free end of the mechanical stopper in Fig. 1 (a) as a lumped spring-damper system [37], shown in Fig. 3. In other words, the magnitude of the downward impact force exerted by the stopper on the connection point of beam Segment 1 is the same as that of a spring force with a spring constant of K and a damping coefficient, C. Besides impact, it should be noted that the Cu electrode exerts a downward force on the connection point due to gravity. Such a downward force is treated as an equivalent weight roughly equal to half the weight of the Cu electrode and added to the weight of the tip mass, M_1, in the model because the connection point is effectively above M_1. In the derivation of the equations of motion for the LBMS in Fig. 3 the Euler-Bernoulli beam theory is used. The equations for the LBMS's free vibration are [4]

$$\rho_1 \ddot{y}_1(x_1,t) + E_1 I_1 \frac{d^4}{dx_1^4} y_1(x_1,t) = 0 \tag{9}$$

$$\rho_2 \ddot{y}_2(x_2,t) + E_2 I_2 \frac{d^4}{dx_2^4} y_2(x_2,t) + M_2 g \frac{d^2}{dx_2^2}(x_2,t) = 0 \tag{10}$$

$$\rho_3 \ddot{y}_3(x_3,t) + E_3 I_3 \frac{d^4}{dx_3^4} y_3(x_3,t) = 0 \tag{11}$$

where ρ_1, ρ_2, and ρ_3 are the mass densities per unit length of beam Segments 1, 2, and 3; E_1, E_2, and E_3 are the Young's Moduli of beam Segments 1, 2, and 3, respectively; I_1, I_2, and I_3 are the second moments of area of beam Segments 1, 2, and 3, respectively; g is the gravitational acceleration; $y_1(x_1,t)$, $y_2(x_2,t)$, and $y_3(x_3,t)$ are the displacements of the beam segments in their respective coordinate systems. The essential boundary conditions are

$$\begin{gathered} y_1(0,t) = 0,\ y_2(0,t) = 0,\ \frac{d}{dx_1} y_1(0,t) = 0,\ \frac{d}{dx_2} y_2(0,t) = \frac{d}{dx_1} y_1(L_1,t), \\ y_3(0,t) = y_2(L_2,t),\ \frac{d}{dx_3} y_3(0,t) = \frac{d}{dx_2} y_2(L_2,t) \end{gathered} \tag{12}$$

where L_1, L_2, and L_3 are the lengths of beam Segments 1, 2, and 3, respectively. The equilibrium relations of moment and shear force at the ends of the beam segments are derived as

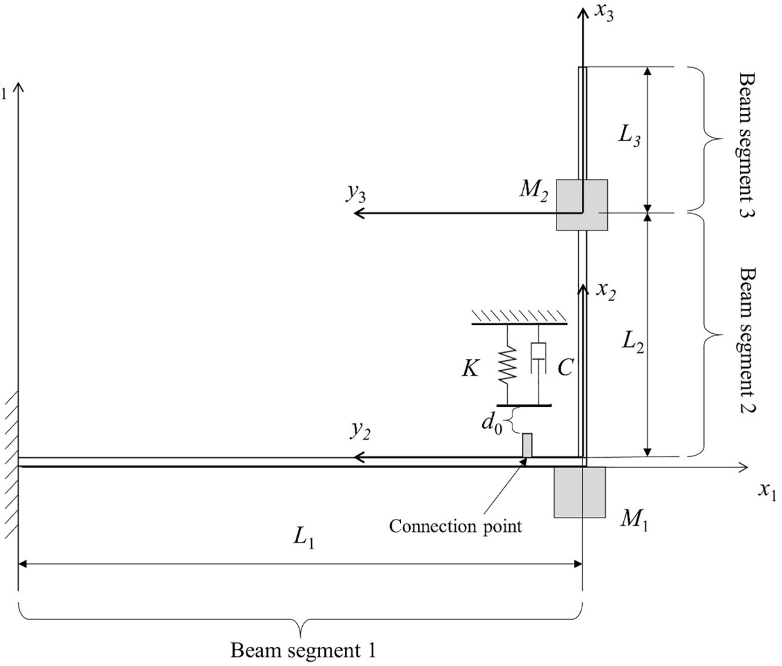

Fig. 3. The mechanical model of the LTEH.

$$E_1I_1\frac{d^2}{dx_1^2}y_1(L_1,t)=E_2I_2\frac{d^2}{dx_2^2}y_2(0,t) \tag{13}$$

$$E_2I_2\frac{d^2}{dx_2^2}y_2(L_2,t)=E_3I_3\frac{d^2}{dx_3^2}y_3(0,t) \tag{14}$$

$$E_1I_1\frac{d^3}{dx_1^3}y_1(L_1,t)=(\rho_2L_2+\rho_3L_3+M_1+M_2)\ddot{y}_1(L_1,t) \tag{15}$$

$$E_2I_2\frac{d^3}{dx_2^3}y_2(L_2,t)=M_2\left[\ddot{y}_2(L_2,t)-g\frac{d}{dx_2}y_2(L_2,t)\right]+E_3I_3\frac{d^3}{dx_3^3}y_3(0,t) \tag{16}$$

$$E_3I_3\frac{d^2}{dx_3^2}y_3(L_3,t)=0 \tag{17}$$

$$E_3I_3\frac{d^3}{dx_3^3}y_3(L_3,t)=0 \tag{18}$$

Eqs. (12)-(18) form the boundary conditions for the equations of motion. The expansion theorem allows the motion of the L-shape beam to be written as

$$y_i(x_i,t)=\sum_{r=1}^{\infty}Y_{ir}(x_i)\eta_r(t),\ \ i\in\{1,2,3\} \tag{19}$$

where $Y_{ir}(x_i)$ and $\eta_r(t)$ are the eigenfunctions and modal coordinates of the r - th mode of the i - th beam segment, respectively. In Eq. (19), only the steady-state response is considered, so $\eta_r(t)\ = Ae^{i\omega_r t}$. The eigenfunctions are in the forms of

$$Y_{1r}(x_1)=A_{1r}(\sin\beta_{1r}x_1-\sinh\beta_{1r}x_1)+B_{1r}(\cos\beta_{1r}x_1-\cosh\beta_{1r}x_1) \tag{20}$$

$$Y_{2r}(x_2)=A_{2r}\sin\beta_{2r}x_2+B_{2r}(\cos\beta_{2r}x_2-\cosh\beta_{3r}x_2)+C_{2r}\sinh\beta_{3r}x_2 \tag{21}$$

$$Y_{3r}(x_3)=A_{3r}\sin\beta_{4r}x_3+B_{3r}\cos\beta_{4r}x_3+C_{3r}\sinh\beta_{4r}x_3+D_{3r}\cosh\beta_{4r}x_3 \tag{22}$$

where β_{ir} are

$$\beta_{1r}^4=\frac{\omega_r^2\rho_1}{E_1I_1} \tag{23}$$

$$\beta_{2r}^2=\frac{M_2g}{2E_2I_2}+\sqrt{\frac{M_2^2g^2}{4E_2^2I_2^2}+\frac{\rho_2\omega_r^2}{E_2I_2}} \tag{24}$$

$$\beta_{3r}^2=-\frac{M_2g}{2E_2I_2}+\sqrt{\frac{M_2^2g^2}{4E_2^2I_2^2}+\frac{\rho_2\omega_r^2}{E_2I_2}} \tag{25}$$

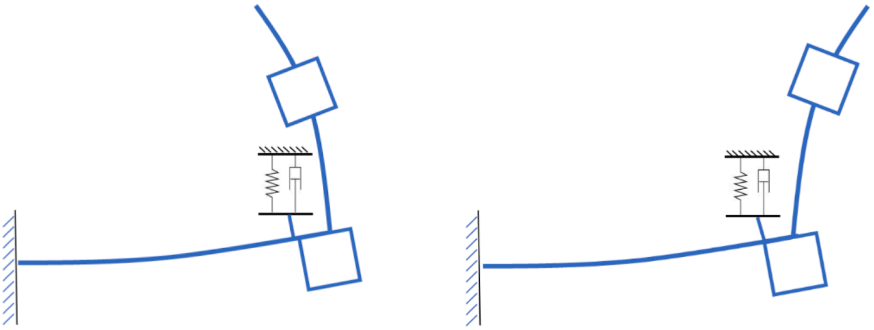

(a) (b)

Fig. 4. Modes shapes of the (a) first mode and (b) second mode.

$$\beta_{4r}^4 = \frac{\omega_r^2 \rho_3}{E_3 I_3} \tag{26}$$

A_{1r}, B_{1r}, A_{2r}, B_{2r}, C_{2r}, A_{3r}, B_{3r}, C_{3r}, and D_{3r} are constants. These eigenfunctions describe the mode shapes of the LBMS in the spatial space under base excitation. The first two mode shapes are roughly shown in Fig. 4 below. Applying the boundary conditions in Eqs. (12)–(18) to the characteristic equations in Eqs. (20)-(22) results in nine algebraic equations, which can be represented as

$$\mathbf{A}(\omega_r)\overrightarrow{c} = 0 \tag{27}$$

where $\mathbf{A}$ is a 9×9 matrix, and $\overrightarrow{c}$ is a 9×1 vector containing the nine constant coefficients in Eqs. (20)-(22). Values of ω_r that lead to $\det(\mathbf{A}) = 0$ are the modal natural frequencies, which are found numerically. Let

$$\ddot{y}_v(t) = a_{\mathrm{B}} \sin(\omega_v t) \tag{28}$$

be the vertical transverse harmonic base acceleration where a_{B} is the amplitude of the acceleration and ω_v is the excitation frequency. Eq. (28) acts on beam Segment 1, so the forced undamped vibration of it can be represented as

$$\begin{aligned} &\rho_1 \ddot{y}_1(x_1,t) + E_1 I_1 \frac{d^4}{dx_1^4} y_1(x_1,t) = -\rho_1 \ddot{y}_v(t) \\ &-(\rho_2 L_2 + \rho_3 L_3 + M_1 + M_2)\delta(x_1 - L_1)\ddot{y}_v(t) \end{aligned} \tag{29}$$

Inserting Eq. (19) into Eq. (29), multiplying both sides of Eq. (29) by $Y_{is}(x_i)$ where s is a modal number different from r, integrating it over the length of beam 1, and introducing modal damping, give

$$\rho_1 \int_0^{L_1} \sum_{r=1}^{\infty} Y_{1r}(x_1) Y_{1s}(x_1) \ddot{\eta}_r(t) dx_1 + E_1 I_1 \int_0^{L_1} \sum_{r=1}^{\infty} \frac{d^4}{dx_1^4} Y_{1r}(x_1) Y_{1s}(x_1) \eta_r(t) dx_1 = N_r(t) \tag{30}$$

where $N_r(t)$ is the time-dependent modal force. Introducing modal damping with orthogonality between different eigenfunctions gives

$$\ddot{\eta}_r + 2\zeta_r \omega_r \dot{\eta}_r + \omega_r^2 \eta_r(t) = N_r(t) \tag{31}$$

where ζ_r is the modal damping ratio. The modal force can be derived as

$$\begin{aligned} N_r(t) = -&\left[\rho_1 \int_0^{L_1} Y_{1r}(x_1) dx_1 + (\rho_2 L_2 + \rho_3 L_3 + M_1 + M_2) Y_{1r}(L_1)\right] \ddot{y}_v(t) \\ &+ F_{\mathrm{p}r}(t) + F_{\mathrm{e}r}(t) \end{aligned} \tag{32}$$

where $F_{\mathrm{p}r}$ is the modal impact force from the lumped spring-damper stopper when the triboelectric pair is in contact, and $F_{\mathrm{e}r}$ is the modal electrostatic attraction force exerted on the connection point on beam Segment 1. Since the connection point is close to the free end of beam segment 1, the modal impact force can be seen as being exerted on the free end at $x_1 = L_1$. The modal impact force is expressed as

$$F_{\mathrm{p}r} = \begin{cases} 0 & y_1(L_1,t) \leqslant d_0 \\ [K(d_0 - y_1(L_1,t)) - C\dot{y}_1(L_1,t)] Y_{1\mathrm{r}}(L_1) & y_1(L_1,t) > d_0 \end{cases} \tag{33}$$

where d_0 is the initial separation distance between the outer ends of the contact surfaces. Since the electrostatic force is assumed to be distributed on the whole surface of the Cu electrode according to Eq. (7), the location of the equivalent point load can be derived as

$$l_{\mathrm{eq}} = \frac{\int_{l_1 - l_2}^{l_1} l \cdot dF_{\mathrm{e}}}{F_{\mathrm{e}}} = \mu l_2 \tag{34}$$

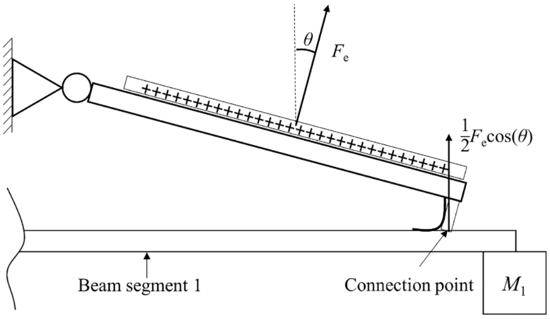

Fig. 5. The equivalent electrostatic force acting on the point of connection between beam segment 1 and the Cu electrode.

As shown in Fig. 5, the force can be treated as acting perpendicularly on the Cu electrode at $l = \mu l_2$. Since the left end of the Cu electrode's substrate rotates freely, the equivalent modal attraction force, $F_{\mathrm{er}}(t)$ on the beam's connection point is

$$F_{\mathrm{er}}(t) = \frac{\mu l_2 F_{\mathrm{e}}\cos(\theta)}{l_1} Y_{1r}(L_1) = \frac{\mu l_2 [\sigma A_{\mathrm{c}} - Q(t)]^2 \cos(\theta)}{2 l_1 A_{\mathrm{c}} \in_0} Y_{1r}(L_1) \tag{35}$$

From Eq. (35), it is clear that the transferred charge $Q(t)$ is the coupling term from the electrical model to the equations of motion here. The gap distance between the tips of the contact surfaces d_{G} is expressed as

$$d_{\mathrm{G}} = \begin{cases} 0 & y_1(L_1, t) \geqslant d_0 \\ d_0 - y_1(L_1, t) & y_1(L_1, t) > d_0 \end{cases} \tag{36}$$

Eq. (36) indicates that the model assumes complete contact between the triboelectric pair when the displacement reaches the initial gap distance d_0 at beam Segment 1′s free end tip. The parameters of the mechanical model used in the simulation and experiment are chosen such that the first two undamped natural frequencies are $f_1 = 7.45$ Hz and $f_2 = 14.39$ Hz under free vibration ($f_2 \cong 2f_1$). The numerical values of these parameters are shown in Table 2.

As a summary, the coupled model consists of Eqs. (31) and (5) as shown below

$$\ddot{\eta}_r + 2\zeta_r \omega_r \dot{\eta}_r + \omega_r^2 \eta_r(t) = -\left[\rho_1 \int_0^{L_1} Y_{1r}(x_1) dx_1 + M Y_{1r}(L_1)\right] \ddot{y}_v(t) + F_{\mathrm{pr}}(t) + F_{\mathrm{er}}(t) \tag{37}$$

$$R\frac{dQ(t)}{dt} = \frac{\mu[\sigma A_{\mathrm{c}} - Q(t)] d_{\mathrm{G}}(t)}{w l_1 \varepsilon_0} - \frac{Q(t) h}{A_{\mathrm{c}} \varepsilon_{\mathrm{r}} \varepsilon_0} \tag{38}$$

where

$$M = \rho_2 L_2 + \rho_3 L_3 + M_1 + M_2 \tag{39}$$

$$F_{pr} = \begin{cases} 0 & y_1(L_1, t) \leqslant d_0 \\ [K(d_0 - y_1(L_1, t)) - C\dot{y}_1(L_1, t)] Y_{1\mathrm{r}}(L_1) & y_1(L_1, t) > d_0 \end{cases}$$

$$F_{\mathrm{e}r}(t) = \frac{\mu l_2 [\sigma A_{\mathrm{c}} - Q(t)]^2 \cos(\theta)}{2 l_1 A_{\mathrm{c}} \varepsilon_0} Y_{1\mathrm{r}}(L_1)$$

$$d_{\mathrm{G}} = \begin{cases} 0 & y_1(L_1, t) \geqslant d_0 \\ d_0 - y_1(L_1, t) & y_1(L_1, t) > d_0 \end{cases}$$

The coupled equations, Eqs. (37) and (38), can be numerically simulated by the ordinary-differential-equation solver, ODE15S, provided by Matlab. Since only the first two modes are excited in practicality, the first three vibration modes are included in the simulation program, with the third included for better convergence.

Table 2
Parameters for the mechanical model used in the simulation and experiment.

Parameters	Values
Length of beam segment 1, L_1	140 mm
Length of beam segment 2, L_2	95 mm
Length of beam segment 3, L_3	39 mm
Young's Modulus of beam segment 1, E_1	21 GPa
Young's Moduli of beam segments 2 and 3, E_2 and E_3	27 GPa
Width of beam segment 1, b_1	30 mm
Widths of beam segments 2 and 3, b_2 and b_3	20 mm
Height of beam segment 1, h_1	1 mm
Heights of beam segments 2 and 3, h_2 and h_3	0.6 mm
Mass density per unit length of beam segment 1, ρ_1	1780 kg/m
Mass densities per unit length of beam segments 2 and 3, ρ_2 and ρ_3	1905 kg/m
Tip mass on beam segment 1, M_1	9.40 g
Proof mass on beam segment 2, M_2	3.03 g
The stopper's equivalent stiffness, K	30000 N/m
The stopper's equivalent damping coefficient, C	0.15

4. Experiment results and model validation

4.1. Experimental setup and preliminary results

Fig. 6 shows the setup of the experiment conducted to validate the theoretical model presented above and characterize the performance of the LTEH. The LTEH is clamped on a shaker that provides vertical harmonic base vibration. The excitation accelerations and frequencies of the vibration can be controlled through a vibration controller that takes feedback from the shaker via an accelerometer glued on the shaker. The vibration controller is operated via a computer software interface. A power amplifier is used to increase the voltage and current of the control signal. The two electrodes of the energy harvesting unit are connected to a data acquisition module with a built-in resistance of 1 MΩ. The acquired data of the voltage response can be viewed from the software that accompanies the data acquisition module.

For a preliminary validation of the LTEH's performance, a frequency sweep from 5.5 Hz to 17 Hz with a sweep speed of 0.1 Hz/s at a constant excitation acceleration of $a_B = 0.4$ g was applied to the shaker. The sweep range was selected to cover the first two natural frequencies of the LTEH. The initial separation distance d_0 was set at 7 mm when the LBMS was in its equilibrium state. The root-mean-squared (RMS) and alternating-current (AC) voltage responses from the LTEH in the frequency sweep are shown in Fig. 7 which shows that the prototype can harvest vibrational energy around the two relatively closely located frequencies below 20 Hz. In Fig. 7 (b), the AC voltage response for the first mode is quite intricate. Periodic ($f = 7.15$–7.25 Hz and $f = 8.15$–8.18 Hz) and quasi-periodic ($f = 7.25$–8.15 Hz) responses are present within this first-mode band. For a detailed investigation into this phenomenon, Fig. 8 (a) shows the detailed waveform consisting of two periods of the voltage response at $f = 7.6$ Hz in the time history, while Fig. 8 (b) shows the different stages of the vibration process of the LBMS corresponding to the left period. Here, v_1 and v_2 denote the velocities of beam Segments 1 and 2, respectively. The first mode shape of the LBMS shown in Fig. 4 (a) indicates that v_1 and v_2 have the same sign in their corresponding coordinate systems defined in Fig. 3 in free vibration. During stage 1, the upward-moving Segment 1 causes the triboelectric pair's contact surfaces to approach each other and increase the voltage. The two surfaces then contact each other, and the positive maximum voltage is reached. In stage 2, Segment 1 starts moving downward due to impact, and the voltage drops quickly because of reverse charge transfer. However, Segment 2 does not stop moving leftward because of its inertia and exerts a counterclockwise moment at the free end of Segment 1. This moment brings the free end of Segment 1 up again and induces a minor increase in voltage in stage 3. Afterward, both beam segments start moving in the negative direction in stage 4, where the negative voltage peak is reached. Essentially, the opposing moment exerted by Segment 2 during stage 3 decreases the kinetic energy of the beam-mass structure, so the next period in stage 5 has smaller voltage peaks. The energy loss and instability due to impact also contribute to the maximum RMS voltage at the first mode being lower even though the magnitude of the AC voltage is larger.

Because the first two natural frequencies here satisfy $f_2 \cong 2f_1$, modal energy exchange due to nonlinear internal resonance might occur and contribute to the instabilities displayed in Fig. 7 (b). However, when d_0 is increased to 11 mm, the instabilities disappear when at the first mode for the same excitation acceleration of 0.4 g, as shown in Fig. 9. Thus, the destabilizing effect due to internal resonance is absent here and is only due to the increased magnitude of impact.

Preliminary validation of the theoretical model that simulated a frequency sweep with the same vibration parameters was conducted in Matlab. From Eqs. (5) and (31)-(35), the governing equation of the mechanical system is non-smooth, and both the mechanical and electrical systems are possibly stiff due to small constants such as ε_0. Therefore, ODE15s is chosen to solve the differential equations in Matlab with the Jacobian matrix of the governing equations supplied to improve the computational reliability and speed. The surface charge density per unit area σ used in the model was 35.7 $\mu C/m^2$, which was determined by taking the maximum transferred charge Q_{max} measured by an electrometer and dividing it by the contact surface area A_c. It should be noted that, although the areal charge density on the PTFE dielectric layer is constant, the charge density induced on the copper layer when in contact with

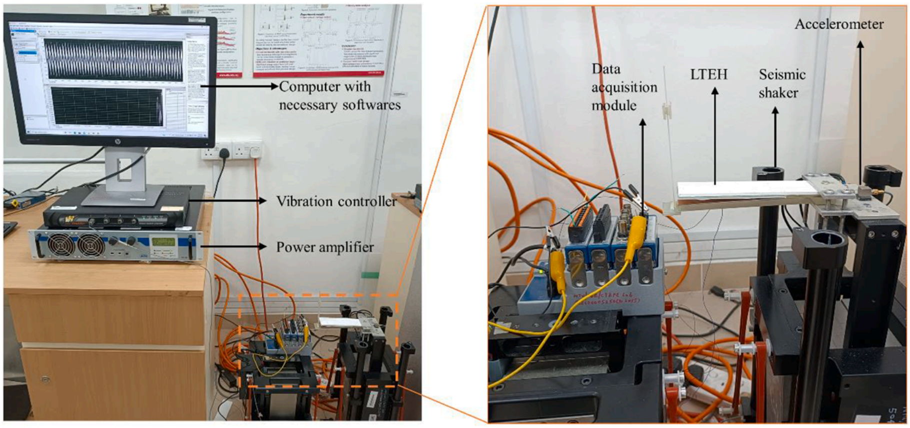

Fig. 6. The experimental setup with the LTEH, seismic shaker, accelerometer, and data acquisition module (right) and the complete setup with the power amplifier, vibration controller, and computer with the necessary software (left).

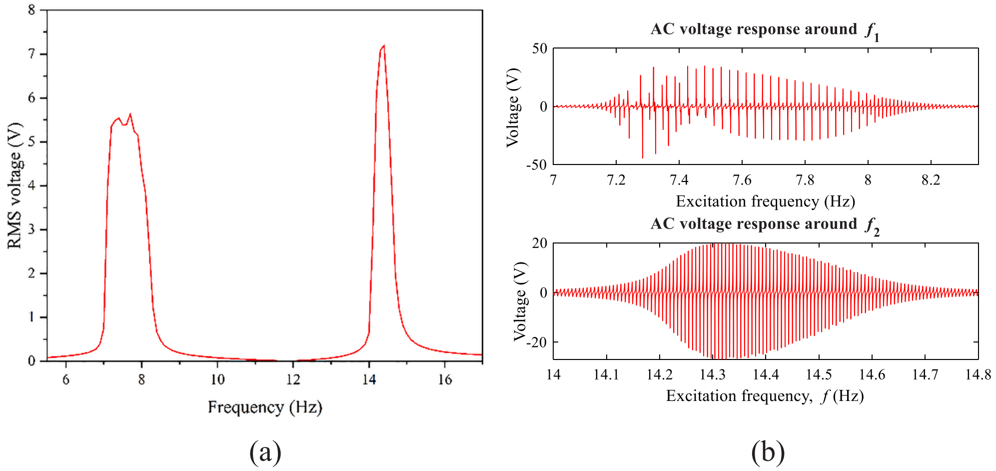

Fig. 7. (a) RMS voltage response and (b) AC voltage responses around the first two natural frequencies of the LTEH in the frequency domain at a_B = 0.4 g and d_0 = 7 mm.

the PTFE layer is not constant in the experiment depending on the magnitudes of the excitation acceleration and the initial separation distance as they affect how complete the contact is. Therefore, the numerical value of σ set in the simulation program equals the effective charge density acquired on the copper layer when in contact with the PTFE [18], which is different for each excitation acceleration and initial separation distance. The modal damping ratios ζ_r were roughly estimated using the logarithmic decrement method by observing the decay of the strain data of beam Segment 1 when the first two modes were excited by the shaker. Here, for a_B = 0.4 g and $d_0 = 7$ mm, $\zeta_1 = 1.78\%$ and $\zeta_2 = 1.5\%$. Besides, the experimental and simulated AC voltage responses in the time domain at the excitation frequency of $f = 14.4$ Hz were compared. Fig. 10 compares the simulated and experimental results of the RMS voltage and AC voltage responses at $f = 14.4$ Hz, given the vibration parameters in the last paragraph.

Good agreement is observed between the simulated and experimental data under the specified vibration conditions. As shown in Fig. 10 (a), the predicted operating frequencies of two modes and maximum RMS voltages of the proposed L-shaped LTEH are considerably close to the experimental values. The simulated time-domain AC voltage responses at the second mode in Fig. 10 (b) match well with the experimental results. For the first-mode response, slight overestimations can be seen in the simulated maximum RMS voltage shown in Fig. 10 (a). This can be explained by the stiff impact that causes a loss in the kinetic energy of the LBMS in practicality. The theoretical model here is an idealization, and the energy loss and the instabilities that occur in the first mode are difficult to quantify. From Fig. 7 (b), it is evident that, in the quasi-periodic region of the first-modal AC voltage response (e.g., from f = 7.6 Hz to f = 7.8 Hz), one low-peak period is surrounded by two high-peak periods, which also results in smaller actual first-modal RMS voltage response. Nonetheless, the theoretical model can correctly predict the primary performance characteristics of the LTEH when given the aforementioned vibrational and geometric parameters.

4.2. Parametric studies

Ambient vibrations differ across a wide range of accelerations, so it is necessary to characterize the performance of the proposed LTEH under different excitation accelerations. Therefore, frequency sweeps from 5.5 to 17 Hz with a sweep rate of 0.1 Hz/s under base excitation accelerations (a_B) of 0.3 g, 0.4 g, 0.5 g, and 0.6 g were applied. The initial separation distance d_0 was kept at 7 mm. This configuration is denoted as LTEH-7, where 7 means $d_0 = 7$ mm. Table 3 shows the experimentally determined surface charge densities (σ) and modal damping ratios (ζ_1 and ζ_2) under different base excitation accelerations. Fig. 11 shows the frequency domain's experimental and simulated RMS voltage responses. From Fig. 11, it is evident that the RMS output voltage increases monotonically with base excitation acceleration. A noticeable trend is that the second-mode response decreases more drastically compared to the first-mode response when a_B decreases. This faster decrease occurs because the second mode leads to a smaller $y_1(L_1, t)$ when excited than the first mode, which can be explained by the nature of the second mode shape shown in Fig. 4 (b). When the second mode is excited, beam Segment 2 always exerts a moment opposing the rotational direction at the free end of beam Segment 1 during vibration. Therefore, under small a_B, the triboelectric materials might not contact each other when the second mode is excited, causing small RMS voltage output. However, due to its higher frequency, when a_B increases until the triboelectric materials come into contact, the RMS voltage increases drastically as the AC voltage response in the time history will have more periods. In addition, the first mode results in broader bandwidths because it has a larger displacement amplitude at the free end of beam Segment 1, $y_1(L_1, t)$, given certain excitation acceleration a_B and excitation frequency f. This means that the electrode substrates can contact each other much further away from f_1.

The predicted maximum values of the RMS voltage response in the frequency domain in Fig. 11 (b) show a right-shift phenomenon. The reason for this is that, in the model, the mechanical stopper increases the overall stiffness of the structure during vibration resulting in a slightly increased resonance frequency, as suggested by Eq. (33). In fact, the value of the stopper's equivalent stiffness $K = 30000$

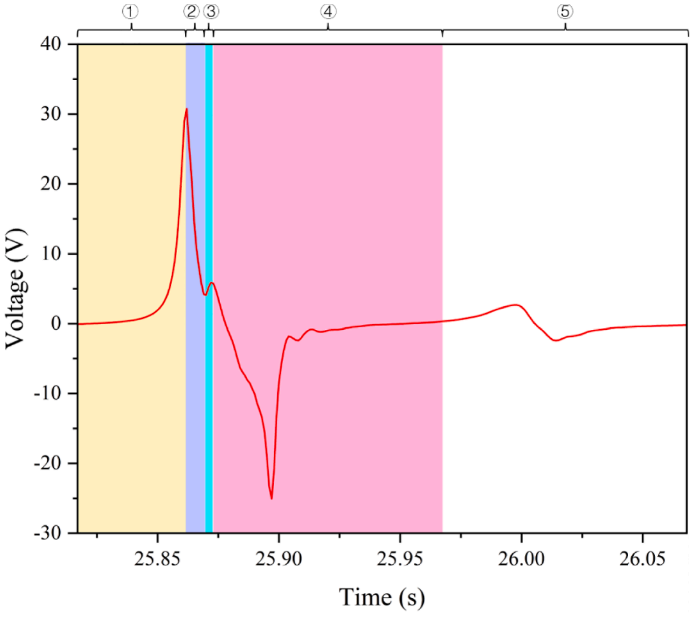

(a)

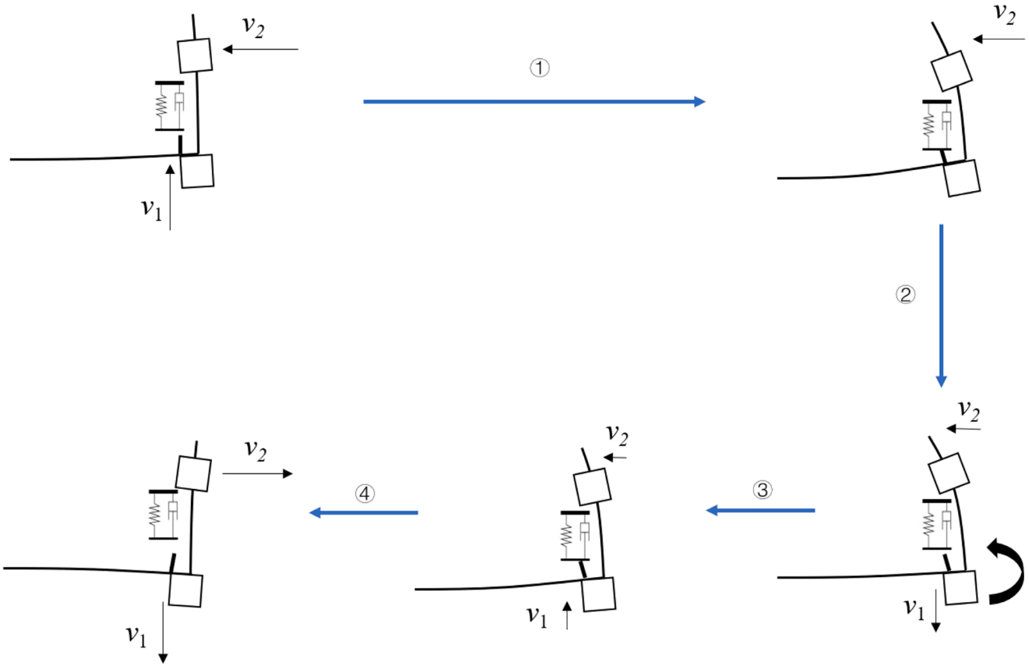

(b)

Fig. 8. (a) The voltage response at $f = 7.6$ Hz. (b) Different stages of the beam-mass structure's vibration process during the left period.

N/m shown in Table 2 was determined by gradually increasing the value of K until the simulated peak of the RMS voltage in the frequency domain of LTEH-7 under $a_B = 0.4$ g was right-shifted until it was centered at the same position as the experimental peak. However, the structural stiffening effect [14,15,26] also shifts the RMS maxima to the right of the peaks, which can be seen in Fig. 12 (a). This effect is more noticeable when the excitation acceleration increases because the Cu electrode experiences a more extended sticking motion with the stopper. In the experiment, on the other hand, damping due to various non-ideal factors prevents the RMS maxima from being right-shifted. For instance, the mechanical stopper's damping coefficient C in Eq. (33) is difficult to quantify due to

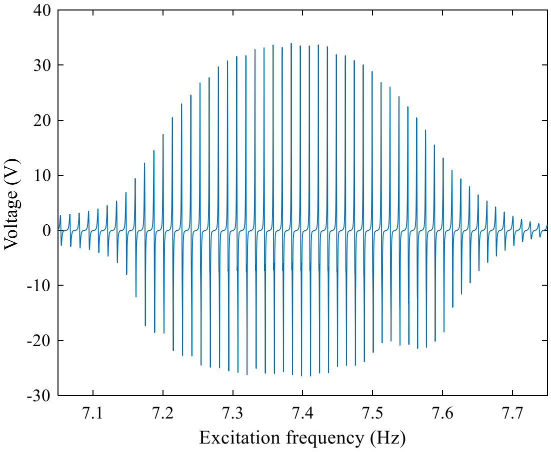

Fig. 9. The AC voltage response around the first natural frequency of the LTEH in the frequency domain at $a_B = 0.4$ g and $d_0 = 11$ mm.

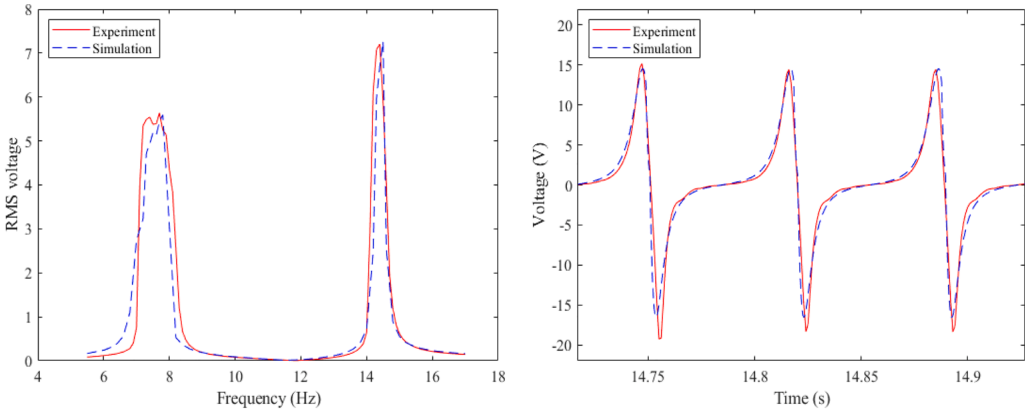

(a) (b)

Fig. 10. (a) Experimental and simulated RMS voltage response and (b) Experimental and simulated AC voltage responses at $f = 14$ Hz at $a_B = 0.4$ g and $d_0 = 7$ mm.

Table 3
Experimentally determined parameters used in the simulation.

a_B	$\sigma(\mu C/m^2)$	ζ_1	ζ_2
0.3	32.89	1.51	1.20
0.4	35.75	1.78	1.23
0.5	39.80	2.02	1.27
0.6	41.23	2.50	1.33

the fabrication process in which the stopper is assembled on the spacer and Al-substrate using double-sided tape that is hypothesized to damp the system significantly. However, Fig. 12 (b) shows that varying C does not substantially affect the RMS voltage response in the frequency domain. Therefore, the value of C was set to 0.15, which was the maximum at which the simulation program did not encounter numerical instabilities. Nonetheless, the centers of the simulated peaks do not deviate much from the experimental data. Besides, each band's predicted maximum RMS voltages agree well with the experimental results.

Another critical parameter that may influence the electrical output of the LTEH is the initial separation distance d_0. By differentiating both sides of Eq. (5) with respect to time, one obtains

$$\frac{\mu[\sigma A_c - Q(t)]}{w l_1 \varepsilon_0}\frac{dd_G(t)}{dt} = R\frac{d^2Q(t)}{dt^2} + \left(\frac{h}{A_c\varepsilon_r\varepsilon_0} + \frac{\mu d_G(t)}{w l_1 \varepsilon_0}\right)\frac{dQ(t)}{dt} \tag{40}$$

This equation indicates that the separation distance's rate of change $\frac{dd_G(t)}{dt}$ is related to the transferred charge's rate of change $\frac{dQ(t)}{dt}$ which

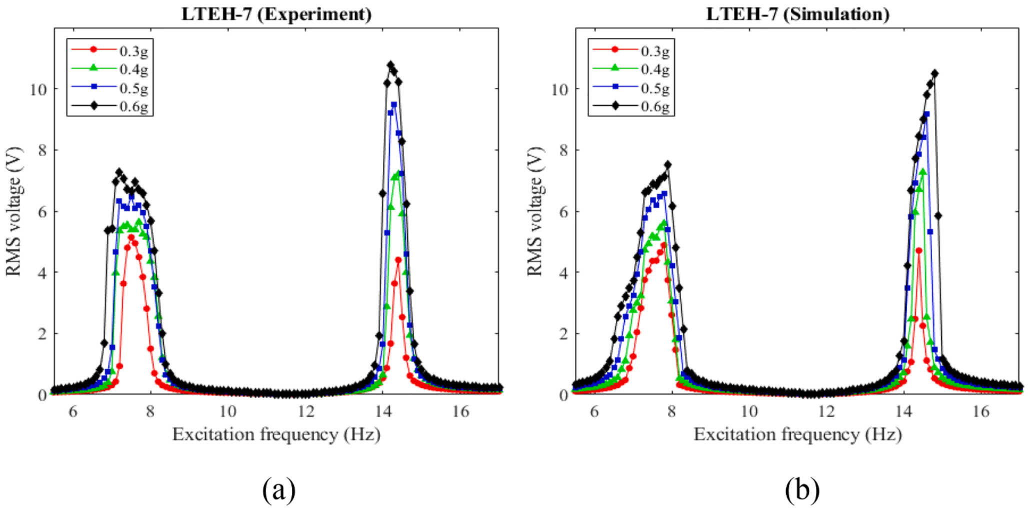

Fig. 11. (a) Experimental and (b) simulated RMS voltage response of LTEH-7 under different base excitation accelerations given $d_0 = 7$ mm.

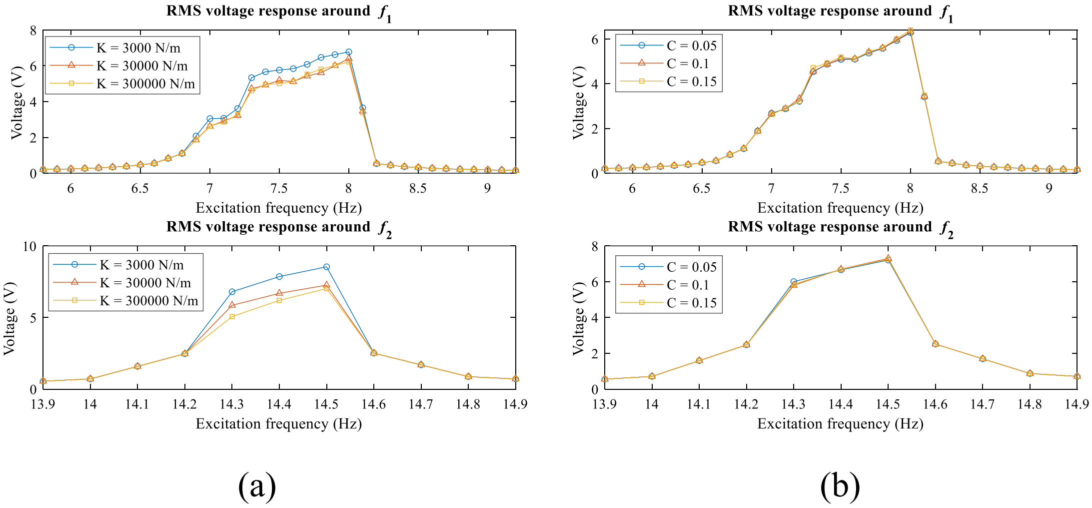

Fig. 12. Simulated RMS voltage responses of LTEH-7 with a base excitation acceleration of 0.4 g given different (a) stopper stiffnesses (K) and (b) stopper damping coefficients (C).

is proportional to the magnitude of the output voltage. Since the magnitudes of the just-before-impact and just-after-impact velocities of the Cu electrode are different due to impact, the positive and negative output voltage peaks in the time domain are different in magnitude, as shown in Fig. 10 (b). The lower positive peaks suggest that the just-before-impact velocity is smaller than the just-after impact one. Therefore, there exists an optimal initial separation distance that maximizes the output RMS voltage since the area under the waveform of the voltage response in the time domain is related to its peak value and rate of change. The just-before-impact velocity being smaller in Fig. 10 (b) is due to the nature of the second mode shape as in Fig. 10 (b), which shows the second-modal AC voltage response in the time domain. The process of the second-modal vibration is shown in Fig. 13. In stage 1, Segment 1 moves upward while Segment 2 moves to the right. Impact takes place for Segment 1 before Segment 2 stops moving to the right. In stage 2, Segment 1 starts moving downward after the impact, but Segment 2 has not stopped moving right and gives the tip of Segment 1 a clockwise moment, which increases the just-after-impact velocity. This faster just-after-impact velocity results in a higher just-after-impact voltage in Fig. 10 (b).

Experiments with various initial separation distances were conducted to find this optimal distance. The chosen values are 5 mm, 7 mm, 9 mm, and 11 mm, which were realized in the experiment by changing the acrylic block with different heights, as shown in Fig. 1 (a). Again, frequency sweeps from 5.5 Hz to 17 Hz were applied to the shaker under excitation accelerations of 0.3 g, 0.4 g, 0.5 g, and 0.6 g for each separation distance. The RMS voltage responses with their corresponding theoretical predictions are shown in Fig. 14. In addition, the first two modal damping ratios, ζ_1 and ζ_2, and surface charge density σ for each case with a specific initial gap distance and excitation acceleration were measured and listed in Table 4.

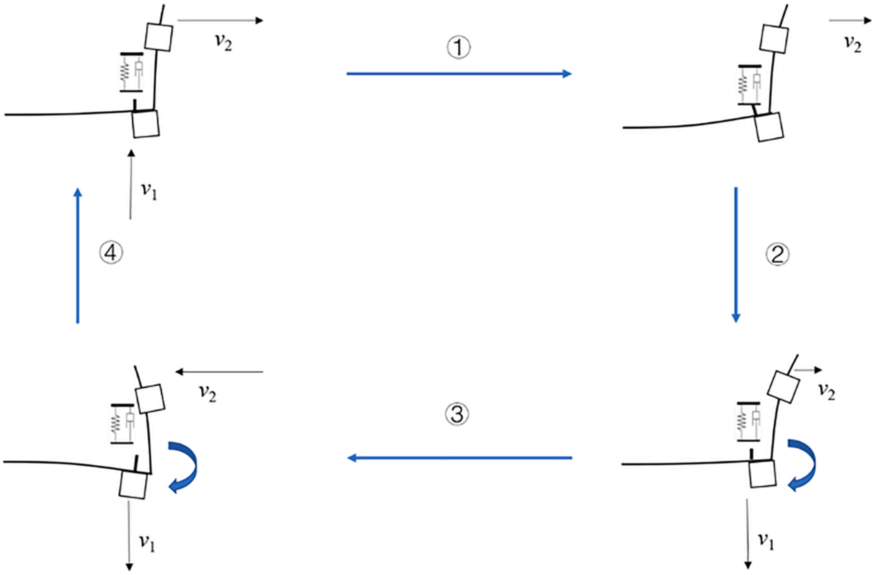

Fig. 13. Different stages of the beam-mass structure's vibration process during a period when the second mode is excited.

Adequately good agreement between the experimental and simulated results can be seen. However, the theoretical model tends to over-predict the right-shifted natural frequencies for smaller d_0. Since, as d_0 decreases, the triboelectric pair's contact surfaces approach each other at higher speeds, the structural stiffening effect due to the stopper is thus larger. This increased stiffening effect is similar to the effect because of increasing excitation accelerations mentioned in Section 4.2. However, characteristic of the first-modal response, the predicted RMS voltages at specific frequencies become more exaggeratedly large for lower d_0 (5 mm). This discrepancy is inherent to the instability-inducing effect of impact, which is difficult to quantify, when the first mode is excited. As shown in Fig. 7 (b) and Fig. 14 (a) and (c), the first-mode response is more susceptible to instability, which is more obvious for smaller initial separation distances and larger excitation accelerations that lead to stronger impact. Nevertheless, main performance characteristics, such as the operating frequencies and maximum RMS voltages, are still correctly predicted for most cases.

From the results shown in Fig. 14, it can be seen that increasing the initial separation distance leads to a decrease in the bandwidths. This is explained by the fact that contact occurs earlier in a vibration cycle when the separation is reduced. In addition, a faster decrease in V_{RMS} for the second peak is observed for increasing d_0 at a given excitation acceleration. This is due to the nature of the second mode shape, whose displacement amplitude at the free end of beam Segment 1 is smaller, as explained in Section 4.2. Therefore, given larger initial separation distances, there may be no contact between the triboelectric pair resulting in smaller V_{RMS}. In contrast, complete contact at the first mode is achieved even for the smallest excitation accelerations at the largest d_0 used in this experiment. This is manifested by the first-mode maximum RMS voltage of LTEH-11 at $a_{\mathrm{B}} = 0.3$ g being larger than that of LTEH-5. The first-modal maximum RMS voltages increase with increasing d_0 because there is less instability and energy loss due to the impact for larger d_0. In addition, as d_0 increases, the time-domain response becomes more stable with fewer or no minor peaks and thus benefits the increase of V_{RMS}. A direct comparison between Fig. 9 and Fig. 7 (b) confirms the above statement. From the observations above, an optimal combination of the excitation acceleration and initial separation distance exists that maximizes the RMS output voltage for each mode. Fig. 15 shows the maximum RMS voltages at each excited mode with varying excitation accelerations. LTEH-11 and LTEH-9 achieve the maximum V_{RMS} for the first-modal and second-modal responses, respectively, given $a_{\mathrm{B}} = 0.6$ g. However, since the maximum second-modal RMS voltage of LTEH-11 is significantly smaller, LTEH-9 operating at $a_{\mathrm{B}} = 0.6$ g was selected in the following performance-characterization experiment.

4.3. Performance characterization

To demonstrate the performance of the LTEH, LTEH-9 was used to charge several capacitors and light several LEDs under the excitation acceleration of 0.6 g. Since real-world energy harvesting devices usually include an energy storage unit consisting of batteries or capacitors, it is crucial to show the prototype's essential capability of charging capacitors. Four capacitors with capacitances 4.7 μF, 10 μF, 22 μF, and 47 μF were chosen for this demonstration. A bridge rectifier that rectifies the alternating-current (AC) voltage output from the LTEH was built to charge each of the four capacitors with full- wave direct-current (DC) voltage without external resistance for 200 s, as shown in Fig. 16. The LTEH was excited at the $f = 7.6$ Hz to charge the capacitors. Then, the same procedure was repeated by exciting the LTEH at $f = 14.3$ Hz. The charging curves showing the voltages across the capacitors over 200 s were recorded using an oscilloscope and are given in Fig. 17. Over the 200 s, the LTEH could charge four capacitors with $C = 4.7$ μF, 10 μF, 22 μF, and 47 μF to 41.32 V, 37.86 V, 20.53 V, and 6.09 V, respectively, at the excitation frequency of $f = 7.6$ Hz. Finally, at $f = 14.3$ Hz, the four capacitors were charged up to 44.65 V, 42.41 V, 22.55 V, and 6.77 V, respectively. Since many IoT sensors can be actuated when a

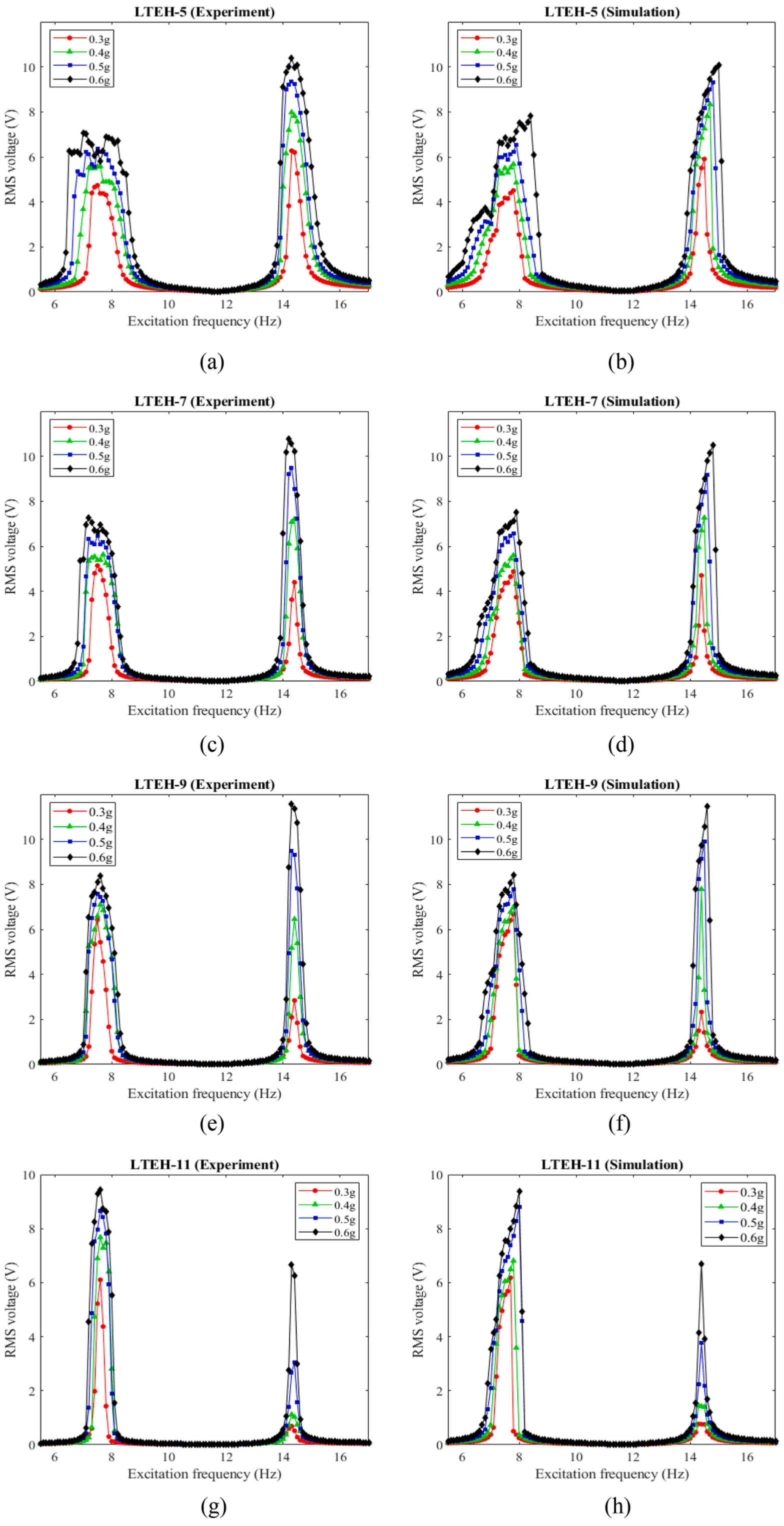

(a) (b)

(c) (d)

(e) (f)

(g) (h)

Fig. 14. The experimental and simulated RMS voltage response of LTEH with initial separation distances under different base excitation accelerations.

Table 4
Experimentally determined parameters used in the simulation.

a_B (g)	d_0 (mm)	σ (μC/m^2)	ζ_1 (%)	ζ_2 (%)
0.3	5	33.37	1.66	1.20
0.3	7	32.89	1.51	1.14
0.3	9	41.71	1.20	1.12
0.3	11	38.13	1.15	1.12
0.4	5	39.09	1.86	1.23
0.4	7	35.75	1.78	1.17
0.4	9	41.71	1.54	1.15
0.4	11	38.13	1.35	1.13
0.5	5	40.52	2.75	1.27
0.5	7	39.80	2.00	1.20
0.5	9	44.09	1.84	1.20
0.5	11	41.23	1.54	1.19
0.6	5	41.70	3.00	1.33
0.6	7	41.23	2.80	1.21
0.6	9	45.28	2.05	1.20
0.6	11	42.90	1.82	1.20

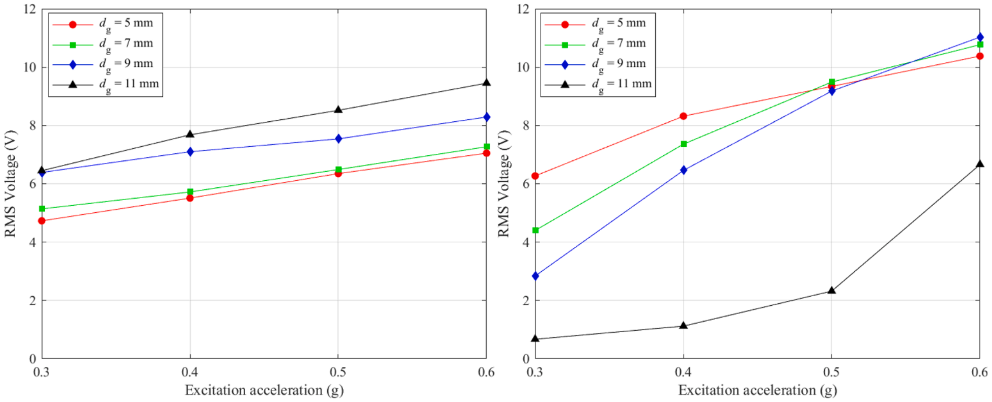

(a) (b)

Fig. 15. Maximum RMS voltages at each excitation accelerations of (a) the first-mode response and (b) the second-mode response.

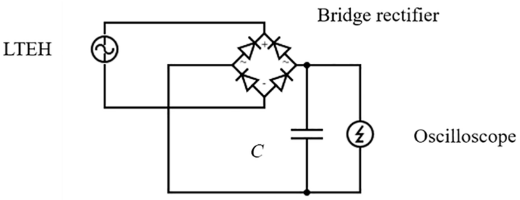

Fig. 16. The circuit diagram for the capacitor charging experiment.

capacitor on the μF scale in its energy storage unit is charged to a voltage in the range of 3–5 V, the LTEH presented in this study can provide many electronic sensors with sufficient energy. LEDs were also used for the performance characterization because they provide a more visual way of recognizing the LTEH's performance. Therefore, the capacitor in the above circuit was replaced with 21 LEDs, which were lit up at both the excitation frequencies shown in Fig. 18 with no visible difference in brightness.

According to Eq. (5), the output voltage depends on both the rate of transfer of the charges, $\frac{dQ(t)}{dt}$, between the electrodes, and the external load R. However, the voltage does not increase monotonically with increasing R as both $\frac{dQ(t)}{dt}$ and $Q(t)$ are influenced by R. Therefore, there exists an optimal external resistance load R_{op} that maximizes the output power P across the load. This optimal resistance load was found experimentally by replacing the capacitor in Fig. 16 with a variable resistor box. Firstly, LTEH-9 was given excited at $f = 14.3$ Hz and connected across a resistance box whose resistance value can be adjusted. The data acquisition module was then connected in parallel to the resistance box to measure the RMS voltage V_{RMS} across the resistance box. The power across the R is

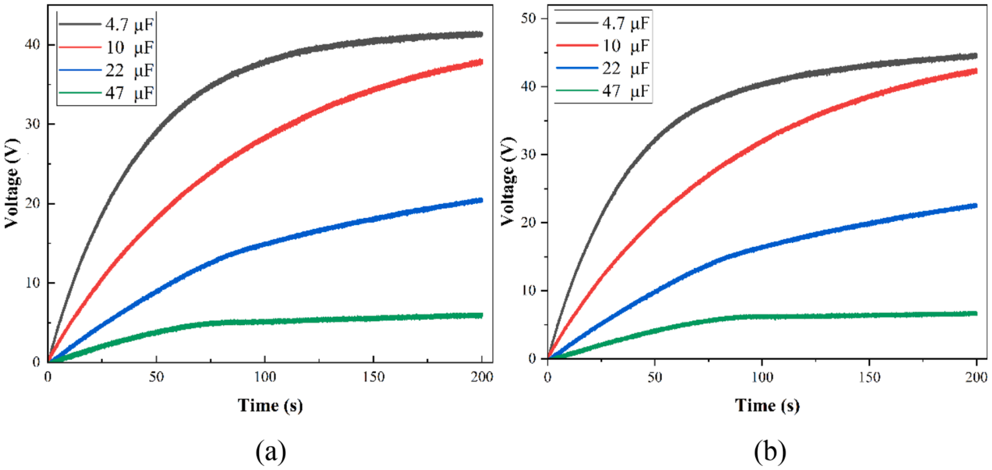

Fig. 17. Capacitor charging curves for the four capacitors with LTEH-9 as the energy harvester under a base excitation acceleration of 0.6 g with excitation frequencies of (a) $f = 7.6$ Hz and (b) $f = 14.3$ Hz.

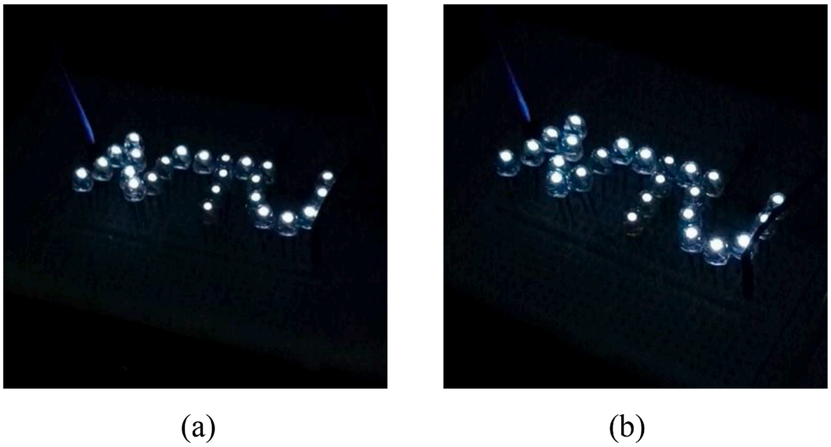
(a) (b)

Fig. 18. LTEH-9 lighted up 21 LEDs under a base excitation acceleration of 0.6 g with excitation frequencies of (a) $f = 7.6$ Hz and (b) $f = 14.3$ Hz.

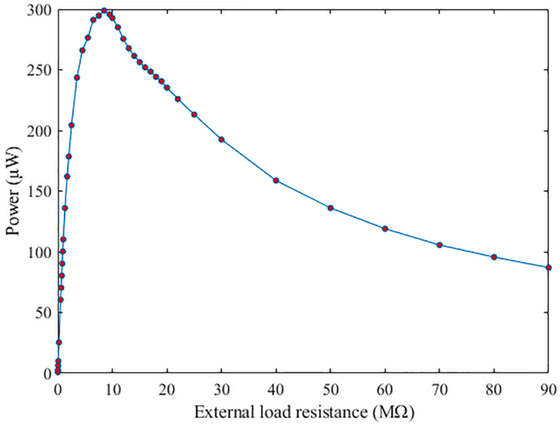

Fig. 19. Output power across various resistances.

calculated as

$$P = \frac{V_{\mathrm{RMS}}^2}{R} \tag{41}$$

The corresponding output power given different R is shown in Fig. 19. The optimal output power of 300 W was achieved when $R = 8.5$ MΩ (Fig. 19). From the optimal output power, the optimal power density per unit volume can be found to be 357.5 μW/cm^3 by taking into account of the volume of the triboelectric materials, which is 0.8392 cm^3.

5. Conclusions

The structural design, theoretical modeling, and experimental validation of a novel triboelectric energy harvester based on an L-shaped beam-mass structure (LTEH) working in the contact-separation mode are presented in this paper. First, the description of the configuration and design of the LTEH is given, followed by its electromechanical model. Next, the mechanical model treats the impact with the mechanical stopper as a stiff spring-damper system and models the LBMS using a distributed parameter model. Afterward, this model is coupled with the electrical model that predicts the output voltage of the LTEH across an external load. Finally, experiments were conducted to validate the derived model and characterize the prototype's performance. The experimental results show satisfactory agreement with the simulated results from the model and the capability of the LTEH to work at two bands in the low-frequency range compared to a single-DOF energy harvesting system due to its relatively close first two natural frequencies. The primary conclusions of this paper are summarized as follows:

- For the first time, the LBMS is introduced as the driving structure for a TEH enabling the use of the second vibration mode as an effective triboelectric energy harvesting mode along with the first mode in the ambient frequency range.
- The expression for the electrostatic attraction force between two non-parallel capacitive plates is derived and incorporated into the theoretical model for the first time for complete coupling and better accuracy. In addition, the model can capture the important performance characteristics of the LTEH considered in the design, such as the operating frequencies, RMS output voltages in the frequency domain, and steady-state output voltage in the time domain.
- The excitation acceleration and initial separation distance between the substrates of the triboelectric pair influence the performance characteristics of the LTEH. Larger excitation accelerations increase the output RMS voltage and operating bandwidth when the harvester is given a specific initial separation distance. However, larger excitation accelerations cause more unstable first modal responses.
- The initial separation distance also affects the magnitude of the output voltage because it affects how much the just-before-impact and just-after-impact velocities of the Cu electrode differ. Besides, larger initial separation distances can also mitigate the instability in the first-modal response. Nonetheless, initial separation distances that are too large can be deleterious to the second modal response as the second-mode maximum displacement amplitude is smaller. Therefore, selecting the optimal parameters when designing the LTEH to work in different conditions is important.
- The LTEH's performance can meet the power requirement for many small electronic sensors, shown by a series of performance characterization experiments with the optimal parameters. The optimal output power of the LTEH is determined to be 300 μW when given an external load resistance of 85 MΩ.

Declaration of Competing Interest

The authors declare that they have no known competing financial interests or personal relationships that could have appeared to influence the work reported in this paper.

Data availability

Data will be made available on request.

References

[1] Y. Pan, et al., Modeling and field-test of a compact electromagnetic energy harvester for railroad transportation, Appl. Energy 247 (2019) 309–321.
[2] H. Honma, Y. Tohyama, H. Mitsuya, G. Hashiguchi, H. Fujita, H. Toshiyoshi, A power-density-enhanced MEMS electrostatic energy harvester with symmetrized high-aspect ratio comb electrodes, J. Micromech. Microeng. 29 (8) (2019), 084002.
[3] Z. Wang, T. Li, Y. Du, Z. Yan, T. Tan, Nonlinear broadband piezoelectric vibration energy harvesting enhanced by inter-well modulation, Energ. Conver. Manage. 246 (2021), 114661.
[4] A. Erturk, J.M. Renno, D.J. Inman, Modeling of piezoelectric energy harvesting from an L-shaped beam-mass structure with an application to UAVs, J. Intell. Mater. Syst. Struct. 20 (5) (2009) 529–544.
[5] W. Guo, et al., Variable stiffness triboelectric nano-generator to harvest high-speed railway bridge's vibration energy, Energ. Conver. Manage. 268 (2022), 115969.
[6] Z.L. Wang, Triboelectric nanogenerators as new energy technology for self-powered systems and as active mechanical and chemical sensors, ACS Nano 7 (11) (2013) 9533–9557.
[7] F.-R. Fan, Z.-Q. Tian, Z.L. Wang, Flexible triboelectric generator, Nano Energy 1 (2) (2012) 328–334.
[8] Q. Shi, T. He, C. Lee, More than energy harvesting–Combining triboelectric nanogenerator and flexible electronics technology for enabling novel micro-/nano-systems, Nano Energy 57 (2019) 851–871.

[9] W. Tang, et al., Liquid-metal electrode for high-performance triboelectric nanogenerator at an instantaneous energy conversion efficiency of 70.6%, Adv. Funct. Mater. 25 (24) (2015) 3718–3725.

[10] Y. Xie, et al., Grating-structured freestanding triboelectric-layer nanogenerator for harvesting mechanical energy at 85% total conversion efficiency, Adv. Mater. 26 (38) (2014) 6599–6607.

[11] S. Niu, et al., Theoretical study of contact-mode triboelectric nanogenerators as an effective power source, Energ. Environ. Sci. 6 (12) (2013) 3576–3583.

[12] L. Zhou, D. Liu, J. Wang, Z.L. Wang, Triboelectric nanogenerators: fundamental physics and potential applications, Friction 8 (3) (2020) 481–506.

[13] B. Yang, W. Zeng, Z.H. Peng, S.R. Liu, K. Chen, X.M. Tao, A fully verified theoretical analysis of contact-mode triboelectric nanogenerators as a wearable power source, Adv. Energy Mater. 6 (16) (2016) 1600505.

[14] L. Dhakar, H. Liu, F. Tay, and C. Lee, “A wideband triboelectric energy harvester,” in *J. Phys.: Conf. Ser.*, 2013, vol. 476, no. 1: IOP Publishing, p. 012128.

[15] C. Zhao, Y. Yang, D. Upadrashta, L. Zhao, Design, modeling and experimental validation of a low-frequency cantilever triboelectric energy harvester, Energy 214 (2021), 118885.

[16] T. Quan, Y. Wu, Y. Yang, Hybrid electromagnetic–triboelectric nanogenerator for harvesting vibration energy, Nano Res. 8 (10) (2015) 3272–3280.

[17] J. Yang, et al., Broadband vibrational energy harvesting based on a triboelectric nanogenerator, Adv. Energy Mater. 4 (6) (2014) 1301322.

[18] Y. Fu, H. Ouyang, R.B. Davis, Triboelectric energy harvesting from the vibro-impact of three cantilevered beams, Mech. Syst. Sig. Process. 121 (2019) 509–531.

[19] Y. Xie, et al., Rotary triboelectric nanogenerator based on a hybridized mechanism for harvesting wind energy, ACS Nano 7 (8) (2013) 7119–7125.

[20] T. Jiang, Y. Yao, L. Xu, L. Zhang, T. Xiao, Z.L. Wang, Spring-assisted triboelectric nanogenerator for efficiently harvesting water wave energy, Nano Energy 31 (2017) 560–567.

[21] X. Fan, J. Chen, J. Yang, P. Bai, Z. Li, Z.L. Wang, Ultrathin, rollable, paper-based triboelectric nanogenerator for acoustic energy harvesting and self-powered sound recording, ACS Nano 9 (4) (2015) 4236–4243.

[22] J. Chen, et al., Harmonic-resonator-based triboelectric nanogenerator as a sustainable power source and a self-powered active vibration sensor, Adv. Mater. 25 (42) (2013) 6094–6099.

[23] S. Anton, A. Erturk, D. Inman, Piezoelectric energy harvesting from multifunctional wing spars for UAVs: Part 2. experiments and storage applications, in: Active and Passive Smart Structures and Integrated Systems 2009, vol. 7288, International Society for Optics and Photonics, 2009, p. 72880D.

[24] H. Wu, L. Tang, Y. Yang, C.K. Soh, A novel two-degrees-of-freedom piezoelectric energy harvester, J. Intell. Mater. Syst. Struct. 24 (3) (2013) 357–368.

[25] D. Upadrashta, Y. Yang, Trident-shaped multimodal piezoelectric energy harvester, J. Aerosp. Eng. 31 (5) (2018) 04018070.

[26] A. Ibrahim, A. Ramini, S. Towfighian, Experimental and theoretical investigation of an impact vibration harvester with triboelectric transduction, J. Sound Vib. 416 (2018) 111–124.

[27] Y. Fu, H. Ouyang, R. Benjamin Davis, Nonlinear structural dynamics of a new sliding-mode triboelectric energy harvester with multistability, Nonlinear Dyn. 100 (3) (2020) 1941–1962.

[28] R.K. Gupta, Q. Shi, L. Dhakar, T. Wang, C.H. Heng, C. Lee, Broadband energy harvester using non-linear polymer spring and electromagnetic/triboelectric hybrid mechanism, Sci. Rep. 7 (1) (2017) 1–13.

[29] A. Nayfeh, B. Balachandran, M. Colbert, and M. Nayfeh, “An experimental investigation of complicated responses of a two-degree-of-freedom structure,” 1989.

[30] A. Nayfeh, B. Balachandran, Experimental investigation of resonantly forced oscillations of a two-degree-of-freedom structure, Int. J. Non Linear Mech. 25 (2–3) (1990) 199–209.

[31] B. Balachandran, A. Nayfeh, Nonlinear motions of beam-mass structure, Nonlinear Dyn. 1 (1) (1990) 39–61.

[32] X. Wang, et al., Harvesting ambient vibration energy over a wide frequency range for self-powered electronics, ACS Nano 11 (2) (2017) 1728–1735.

[33] X. Nie, T. Tan, Z. Yan, Z. Yan, M.R. Hajj, Broadband and high-efficient L-shaped piezoelectric energy harvester based on internal resonance, Int. J. Mech. Sci. 159 (2019) 287–305.

[34] A.H. Nayfeh, D.T. Mook, Nonlinear Oscillations ch. 1 (1995) 1–38.

[35] J. Henniker, “Triboelectricity in polymers,” *Nature,* vol. 196, no. 4853, pp. 474-474, 1962.

[36] Z. L. L. Wang, Long; Chen, Jun; Niu, Simiao; Zi, Yunlong, *Triboelectric Nanogenerators*. Springer International Publishing, 2016.

[37] H.-C. Tsai, M.-K. Wu, Methods to compute dynamic response of a cantilever with a stop to limit motion, Comput. Struct. 58 (5) (1996) 859–867.